Additive Manufacturing 15 (2017) 87–92

Contents lists available at ScienceDirect

Additive Manufacturing

journal homepage: www.elsevier.com/locate/addma

Strengthening of ferrous binder jet 3D printed components through bronze infiltration☆

Zachary C. Cordero[a,b,*], Derek H. Siddel[a], William H. Peter[a,b], Amelia M. Elliott[a,b]

[a] Manufacturing Demonstration Facility, Oak Ridge National Laboratory, Knoxville, TN 37932, United States
[b] Materials Science and Technology Division, Oak Ridge National Laboratory, Oak Ridge, TN 37831, United States

ARTICLE INFO

Article history:
Received 26 June 2016
Received in revised form 13 March 2017
Accepted 26 March 2017
Available online 8 April 2017

Keywords:
Powder metallurgy
Microstructure design
Additive manufacturing
Sintering
Infiltration

ABSTRACT

Net-shape 98% dense objects have been fabricated from a rapidly solidified ferrous powder using binder jet 3D printing and molten bronze infiltration. X-ray diffraction, scanning electron microscopy, and differential thermal analysis were used to characterize the structural evolution of the powder feedstock during an infiltration heating cycle. Microindentation and bend tests were performed on the infiltrated material to evaluate its mechanical properties. It was found that infiltration improved the strength of the sintered preforms by eliminating the stress concentration points at interparticle necks.

1. Introduction

Rapidly solidified powders with non-equilibrium microstructures often possess high hardness values and other useful mechanical properties [1]. However, densifying these powders into complex shapes without affecting their structure and unique properties is difficult using traditional processing routes. Pressureless sintering can densify rapidly solidified powders into complex shapes, but achieving full density requires long exposures to elevated temperatures that can cause coarsening and attendant property degradation [2]. Pressure assisted compaction techniques can preserve the microstructure and properties of the feedstock during densification [3–5], but they often yield parts with simple shapes that must be machined prior to use. This introduces new challenges owing to the high hardness of the compacts.

One processing route that can potentially overcome these issues is binder-jet 3D printing followed by melt infiltration. Binder-jet 3D printing is a solid freeform fabrication technique that uses an organic binder to join powder feedstock, layer-by-layer, into a complex shape [6]. Melt infiltration is a densification process in which a molten alloy wicks into a porous preform as a result of capillary forces [7]. When these processes are paired together, they offer two key advantages for the densification of rapidly-solidified powders. First, melt infiltration can densify preforms with centimeter-scale dimensions in a matter of seconds [8]. This means that in most cases of practical interest, melt infiltration requires only a brief thermal excursion that will not harm the microstructure and properties of the feedstock. Second, these processes yield net-shape objects, minimizing the need for subsequent machining and post-processing [9,10].

This paper presents the results of an investigation in which binder jet 3D printing and melt infiltration were used to form and densify a rapidly-solidified ferrous powder. The structural evolution of the powder during an infiltration heating cycle was evaluated using X-ray diffraction, electron microscopy, and thermal analysis. The mechanical properties of the infiltrated material were evaluated using hardness and bend tests. The infiltrated material had a Vickers hardness of 11 GPa, making it well-suited for applications requiring hard net-shape parts.

2. Experimental methods

A 100 kg batch of rapidly solidified powder was prepared using nitrogen gas atomization. The composition of the powder is given in

* Corresponding author at: Department of Materials Science and NanoEngineering, Rice University, Houston, TX 77005, United States.
E-mail address: zachary.cordero@rice.edu (Z.C. Cordero).

http://dx.doi.org/10.1016/j.addma.2017.03.011

Table 1
Composition listed in wt% of the gas-atomized powder.

Fe	Cr	Mo	V	B	C	Si	O
49	18.6	15.8	8.9	3.4	3.3	1.08	0.02

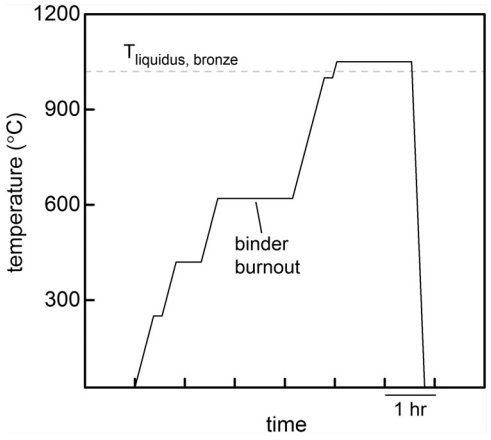

Fig. 1. Heating schedule used with the sintering and the infiltration processes. The isothermal stage at 600 °C is to remove the binder.

Table 1. This alloy was designed so that when it is heated, thermally-stable carbides and borides precipitate and prevent grain growth [11]. The as-received powder was sieved to remove particles with diameters larger than 45 μm since large particles can interfere with printing.

The structure of the powder was characterized using X-ray diffraction (XRD) and scanning electron microscopy (SEM). The XRD patterns were collected on a PANALYTICAL X'Pert PRO diffractometer using Mo Kα radiation. SEM samples were prepared by first mounting the particles in epoxy and then cross-sectioning them using standard metallographic grinding and polishing techniques. The samples were imaged in a Hitachi S3400 scanning electron microscope (SEM) operated at 20 kV and equipped with an energy-dispersive spectroscopy (EDS) detector. The structural evolution of the powder was evaluated using differential thermal analysis (DTA). 120 mg samples were heated to 1300 °C at 10 °C/min in a TA Instruments Q600 under flowing Ar.

An ExOne Lab 3D printer was used to print green parts from the gas-atomized powder. All of the prints were performed using a 100 μm layer thickness and a diethylene glycol binder. After the prints were completed, the binder was cured by heating the entire powder bed to 200 °C for 2 h. The green parts were then de-powdered.

The densification behavior of the 3D printed material was investigated using 6 mm diameter, 8 mm high cylinders printed with their axes of rotation parallel to the build direction. These green bodies were subsequently processed in one of two ways: either they were sintered, or they were infiltrated with tin bronze (Cu-10Sn, wt%). The sintered specimens and the infiltrated specimens were both subjected to the same heating schedule, shown in Fig. 1. This schedule was based on one that had been previously developed for 420 stainless steel powders. It is noted that the 90 minute soak time at the peak temperature in this heating cycle is significantly longer than the time required to infiltrate the preforms. The samples were infiltrated by placing them in direct contact with a reservoir of molten bronze. The sintering and infiltration processes were conducted under flowing Ar + 4% H_2. Following sintering and infiltration, the dimensions of each cylinder were measured at room temperature using a micrometer.

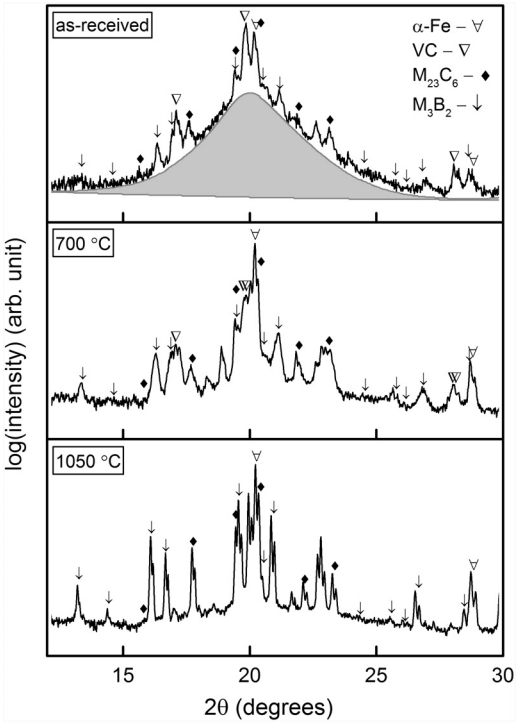

Fig. 2. XRD patterns collected from as-received and annealed powders.

Sintered and infiltrated flat specimens were also prepared for three-point bend tests. The sintered specimens were 6 cm long with cross-sectional dimensions of 4 × 10 mm. The infiltrated specimens had the same initial dimensions as the sintered specimens, but they were ground with SiC papers following infiltration in order to remove the infiltration gating. The final cross-sectional dimensions of the infiltrated specimens were 3.8 × 8.6 mm. The bend tests were performed on a servohydraulic universal test machine. The displacement rate was 0.5 mm/min, the displacement was measured from the crosshead, and the span length was 40 mm in accordance with ASTM C1161. Two bends tests were performed on each material.

These sintered and infiltrated specimens were cross-sectioned and imaged in the same manner as the loose powder particles. In addition, the Vickers microhardness of these cross-sectioned specimens was measured using a LECO microhardness tester with a hold time of 15 s. Low loads (10–50 gf) were used to measure the microhardness values of the individual constituents, while higher loads (5 kgf) were used to measure the effective macrohardness of the composite. A slug of the bronze infiltrant was also cross-sectioned and characterized using microhardness testing.

3. Results and discussion

3.1. Powder structure and properties

Fig. 2 shows an XRD pattern collected from the rapidly-solidified powder particles. The broad low-intensity halo between 15 and 25 °2θ reveals the presence of an amorphous phase. The Bragg peaks overlaid on this halo are assigned to α-Fe, VC, an $M_{23}C_6$ carbide, and an M_3B_2 boride that contains a high concentration of molybdenum.

After sieving, the powder had a mean particle size of 10 μm according to quantitative stereological measurements. The SEM micrograph of two cross-sectioned particles in Fig. 3 shows how the internal structure of the particles depended on their size: the larger particle on the left contains clearly distinguishable regions that correspond to multiple distinct phases, whereas the smaller particle is

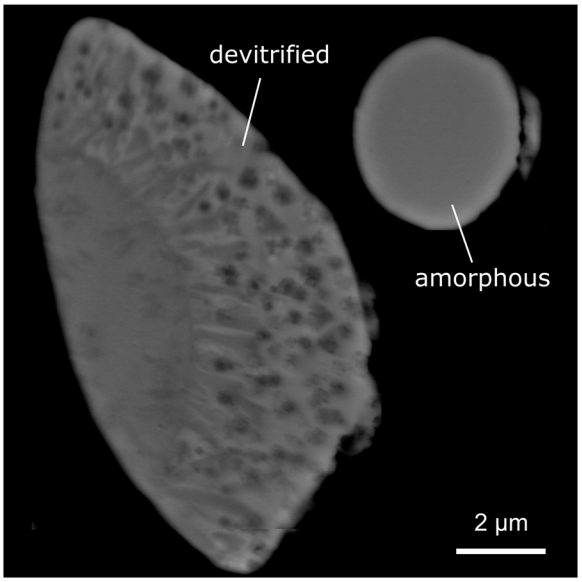

Fig. 3. Electron micrograph of cross-sectioned particles.

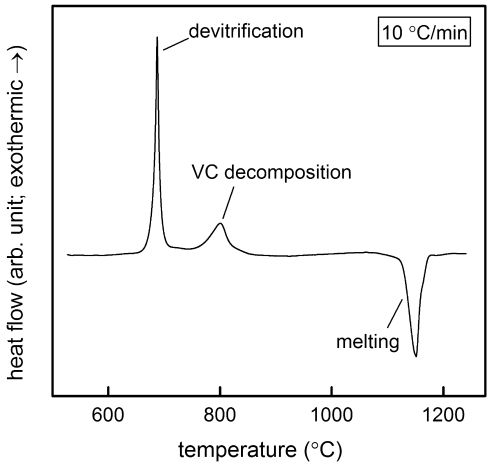

Fig. 4. DTA thermogram collected using a heating rate of 10 °C/min. The exothermic peaks at 690 and 800 °C are associated with devitrification and decomposition of the VC phase, respectively. The endothermic peak at 1150 °C is due to melting.

featureless. Based on the homogeneous structure of these smaller particles, the more rapid cooling rate of finer particles [1], and the broad halo in the XRD pattern, it is inferred that these smaller particles were amorphous. Inspection of many cross-sectioned particles revealed that only particles with diameters less than ~5 μm were fully amorphous.

Fig. 4 shows a representative thermogram from one of the DTA experiments used to study the structural evolution of this alloy. The curve features two irreversible exothermic reactions with peak temperatures at 690 and 800 °C, as well as an endotherm between 1100 and 1180 °C associated with melting. To identify the solid-state reactions associated with each of the exotherms, XRD patterns were collected from powders that had been briefly heated to 700 and 1050 °C. These patterns are presented in Fig. 3, and they show that the exotherm at 690 °C is the result of a devitrification reaction, while the exotherm at 800 °C is due to the decomposition of the VC phase.

Fig. 5 is a high-magnification backscatter electron micrograph of a particle that had been heated to 1050 °C for 90 min, the same temperature and time used in the sintering and infiltration processes. Quantitative EDS showed that the bright regions in Fig. 5

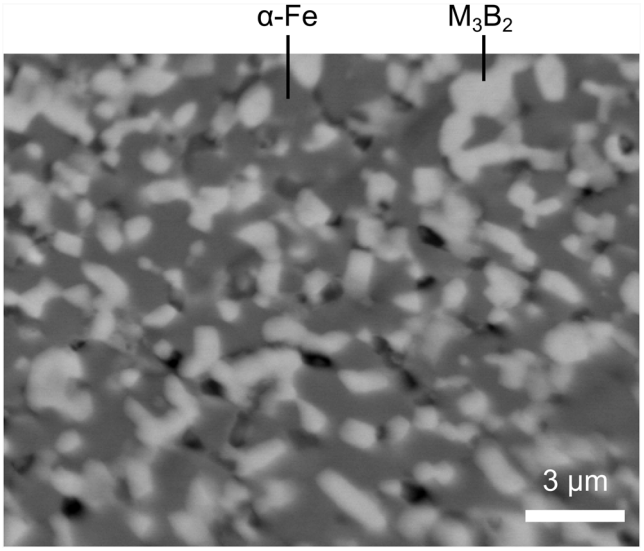

Fig. 5. High-magnification backscatter electron micrograph of a cross-sectioned powder particle that had been held at 1050 °C for 90 min.

were the M_3B_2 boride phase, and that the surrounding matrix was α-Fe. Stereological measurements showed that the volume fraction of the boride phase was 0.2 and that this phase had a mean circular equivalent diameter of 0.5 μm. Using these values with the Zener relation [12], the grain size of the ferrite matrix was estimated to be 3 μm. In light of these results, it seems that this alloy can retain a fine structure even during prolonged exposures to high homologous temperatures. Additionally, all of the annealed particles had a similar structure, so the structural variations seen in the as-received powder must have been eliminated on heating.

3.2. Sintering and infiltration behaviors

The sintered cylinders exhibited a radial shrinkage of 1.1% and an axial shrinkage of 1.4%. This anisotropic shrinkage is likely due to the powder spreading operation, which can orient the particles, leading to anisotropic densification. These results show that this alloy densifies near the liquidus temperature of the bronze infiltrant, which is important since this can help the preform resist slumping during infiltration.

The axial shrinkage of the infiltrated cylinders was 0.7%, half that of the sintered cylinders. Additionally, the infiltrated cylinders swelled 0.4% in the radial direction due to gravitational effects similar to those reported in Ref [13,14]. Quantitative stereological measurements showed that the porosities of the sintered cylinders and the infiltrated cylinders were 33% and 2%, respectively, and that the volume fraction of bronze in the infiltrated cylinders was 0.35.

Fig. 6 is a backscatter electron micrograph of one of the infiltrated cylinders. The bronze infiltrant appears light and the sintered skeleton dark, and there are spherical microvoids randomly distributed throughout both constituents. This micrograph reveals two important features of the infiltrated material. First, there is a several μm-thick denuded zone at the interface between the infiltrant and the sintered skeleton where the α-Fe matrix appears to have dissolved. Second, some regions of the sintered skeleton are free of the boride phase. According to EDS measurements, the composition of these boride-free regions was Fe-6Si-5Cr-5Cu, at%, which is distinct from the nominal composition of the powder feedstock. These two features were only found in the infiltrated specimens, suggesting these boride-free deposits formed because α-Fe dissolved into the molten bronze and then reprecipitated in a second location. This dissolution-precipitation behavior is similar

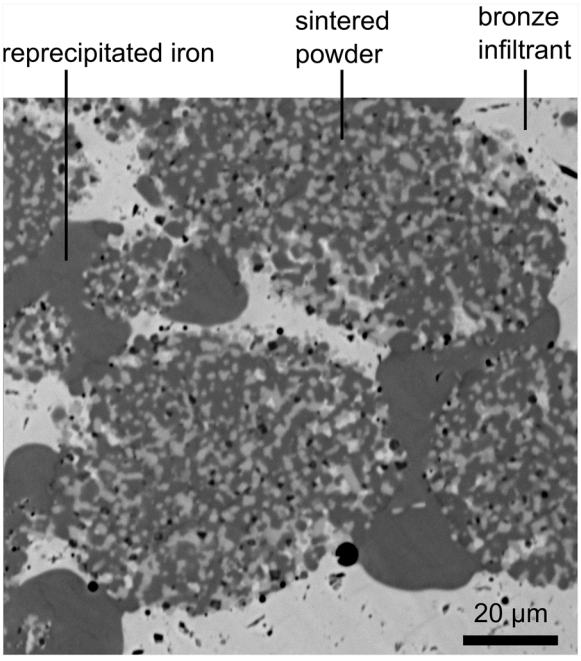

Fig. 6. Backscatter electron micrograph of the infiltrated material.

to that observed in systems that densify by liquid phase sintering [15,16], and is likely driven by the surface energy of the solid particle/molten bronze interface.

3.3. Mechanical properties

The Vickers microhardness of the sintered skeleton was 17 GPa, which, according to the Hall–Petch data in Ref [17], is almost an order of magnitude greater than the expected hardness of pure iron with a grain size of 3 μm. The high hardness of the sintered skeleton relative to that of pure Fe is most likely due to the high volume fraction of the hard boride phase. The macrohardness of the infiltrated material was 11 GPa, or roughly 3 GPa higher than the hardness of as-quenched high strength tool steels (e.g., types M, T, and O) [18]. Further, the macrohardness approximately equals the volume average hardness of the sintered skeleton and the bronze infiltrant, which had a Vickers hardness of 1 GPa.

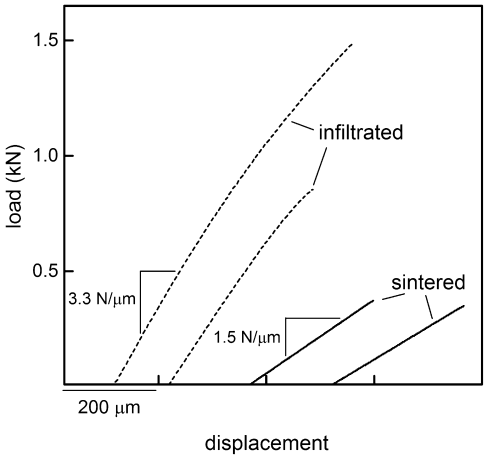

Fig. 7. Load–displacement curves from bend tests on sintered and infiltrated specimens.

Fig. 7 presents load-displacement curves from bend tests on the sintered specimens and the infiltrated specimens. The load-displacement curves from both the sintered and the infiltrated specimens exhibit classic brittle behavior. However, comparison of these load-displacement curves shows that the infiltrated specimens were much stiffer and stronger than the sintered specimens: the infiltrated specimens had an average transverse rupture strength (σ_{TRS}) of 570 MPa, over four times higher than that of the sintered specimens (130 MPa). Still, the infiltrated specimens were weaker than was expected based on their macrohardness values.

The yield strength of the sintered skeleton in both the sintered material and the infiltrated material can be estimated from the bend test results if it is assumed (1) that the bend test specimens fail as soon as the sintered skeleton starts to yield, and (2) that the yield stress of the infiltrated material can be described with an iso-strain model. Under these approximations, the strength of the sintered skeleton in the sintered material (σ_{sint}^{SS}) is given by

$$\sigma_{sint}^{SS} = \frac{\sigma_{TRS}}{(1-P)}, \tag{1}$$

and the strength of the sintered skeleton in the infiltrated material (σ_{inf}^{SS}) is given by

$$\sigma_{inf}^{SS} = \frac{\sigma_{TRS} - f_{Br}\sigma_{Br}}{(1-f_{Br})} \tag{2}$$

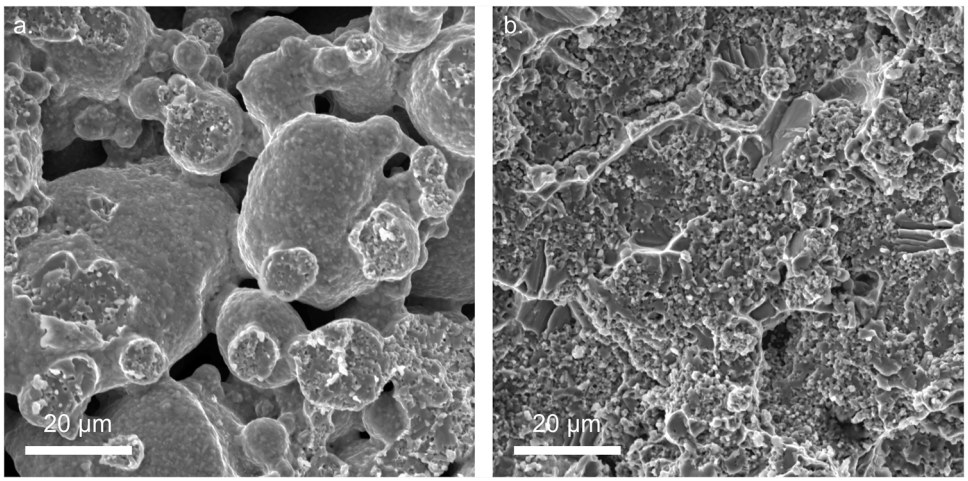

Fig. 8. Electron micrographs of a) a sintered bend-test specimen's fracture surface and b) an infiltrated bend test specimen's fracture surface.

Here, P is the porosity, f_{Br} is the volume fraction of the bronze, and σ_{Br} is the yield stress of the bronze, which can be estimated from the hardness of the bronze (H_{Br}) using the Tabor relation (i.e., $\sigma_{Br} \sim H_{Br}/3$). Using the experimentally determined microstructural parameters and σ_{TRS} values with Eqs. (1) and (2) gives σ_{sint}^{SS} = 190 MPa and σ_{inf}^{SS} = 700 MPa. Thus, infiltration appears to increase the strength of the sintered skeleton by a factor of 3.6.

In order to clarify how infiltration resulted in an almost four-fold increase in the strength of the sintered skeleton, the fracture surfaces of both the sintered and the infiltrated bend test specimens were imaged. The fractograph of a sintered bend test specimen in Fig. 8a shows that this sample failed by brittle fracture at the interparticle necks. In contrast, the fractograph of the infiltrated specimen in Fig. 8b shows that this sample failed primarily by transparticle crack propagation. These disparate failure modes suggest that infiltration increased the strength of the sintered skeleton by eliminating the stress concentration points at the interparticle necks.

Further evidence that this strengthening increment results from eliminating the stress concentration points at the interparticle necks can be obtained by calculating the stress concentration factor (S) at the necks using

$$S \approx 1 + \sqrt{\frac{x}{\rho}} \tag{3}$$

where x is the average neck radius, and ρ is the average radius of curvature of the neck [19]. Quantitative stereological measurements on the sintered specimens gave $x = 4\,\mu m$ and $\rho = 1\,\mu m$, so that $S \approx 3$. Accordingly, Eq (3) predicts that eliminating the stress concentration at the necks should increase the strength of the sintered skeleton by a factor of three, which approximately matches the strengthening increment calculated above.

Closer inspection of the fracture surfaces of the infiltrated specimens revealed two more interesting features. First, the fracture surface contained large cleavage facets, an example of which is shown in Fig. 9a. Using EDS, these regions were identified as the reprecipitated iron deposits. The brittle behavior of these deposits means they should be avoided, and one way to eliminate them is to use a shorter infiltration time. Second, microcracks like the one shown in Fig. 9b intersected the fracture surface in many places. These microcracks had an average length of 15 μm, which is similar to the particle length scale. Because these cracks mostly appeared at the interface between the infiltrant and the sintered skeleton, it seems that the infiltrant played a dual role, simultaneously strengthening the alloy while also introducing crack nucleation sites.

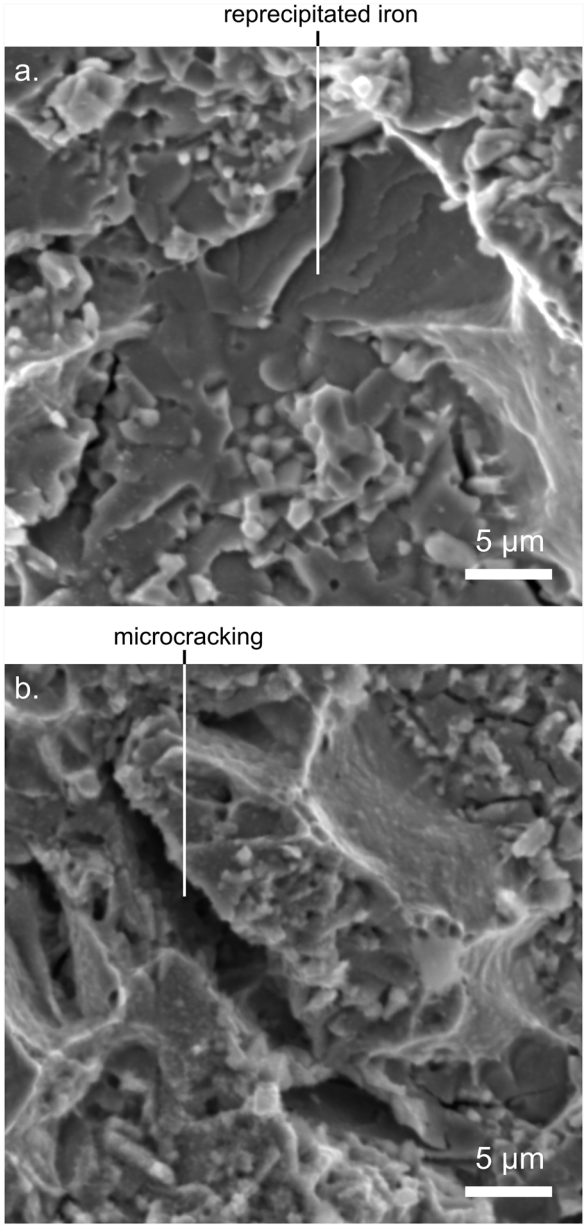

Fig. 9. Electron micrographs of an infiltrated specimen's fracture surface that show a) cleavage facets and b) microcracking.

4. Conclusions

A rapidly-solidified powder was processed using binder-jet 3D printing and molten bronze infiltration. The following conclusions were drawn from a systematic analysis of the microstructure and mechanical properties of the infiltrated material:

- During sintering, the powder feedstock undergoes a series of solid state reactions. The structure that it ultimately develops features a dispersion of sub-micron boride precipitates in an α-Fe matrix.
- During infiltration, some of the α-Fe matrix dissolves into the molten bronze and then re-precipitates at a second location. Inspection of the fracture surface of the infiltrated material showed that this reprecipitated α-Fe was brittle and cleaved, and should therefore be avoided by using shorter infiltration cycles.
- The infiltrated material had a macrohardness of 11 GPa. The transverse rupture strength was 570 MPa which was over four times higher than that of the sintered material. Examination of the fracture surfaces of the sintered material and of the infiltrated material showed that infiltration mainly affected the transverse rupture strength by eliminating the stress concentration points at interparticle necks.
- Applications for the infiltrated material are likely to be in settings where net-shape parts with high hardness values are required.

Acknowledgements

This research was sponsored in part by the U.S. Department of Energy, Office of Energy Efficiency and Renewable Energy, Advanced Manufacturing Office, under contract DE-AC05-00OR22725 with UTBattelle, LLC. The authors thank P. Nandwana, N. Sridharan, F. Montgomery, and S. Hawkins, all of the Oak Ridge National Laboratory, for their assistance with the experiments. References

References

[1] E.Y. Gutmanas, Materials with fine microstructures by advanced powder metallurgy, Progr. Mater. Sci. 34 (4) (1990) 261–366.
[2] G. Thursfield, M.J. Stowell, Mechanical properties of Al-8 wt% Fe-based alloys prepared by rapid quenching from the liquid state, J. Mater. Sci. 9 (10) (1974) 1644–1660.
[3] E. Ayman, U. Junko, K. Katsuyoshi, Application of rapid solidification powder metallurgy to the fabrication of high-strength, high-ductility Mg–Al–Zn–Ca–La alloy through hot extrusion, Acta Mater. 59 (1) (2011) 273–282.
[4] P. Kasiraj, T. Vreeland, R.B. Schwarz, T.J. Ahrens, Shock consolidation of a rapidly solidified steel powder, Acta Metall. 32 (8) (1984) 1235–1241.
[5] N.N. Thadhani, A.H. Mutz, T. Vreeland, Structure/property evaluation and comparison between shock-wave consolidated and hot-isostatically pressed compacts of RSP pyromet 718 alloy powders, Acta Metall. 37 (3) (1989) 897–908.
[6] E.M. Sachs, M.J. Cima, P. Williams, D. Brancazio, J. Cornie, Three dimensional printing: rapid tooling and prototypes directly from a CAD model, J. Eng. Industry 114 (4) (1992) 481–488.
[7] K.A. Semlak, F.N. Rhines, The rate of infiltration of metals, Trans AIME 212 (1958) 325–331.
[8] A.M. Lorenz, E.M. Sachs, S.M. Allen, Freeze-off limits in transient liquid-phase infiltration, Metall. Mater. Trans. A 35 (2) (2004) 641–653.
[9] S. Michaels, E.M. Sachs, M.J. Cima, Metal parts generation by three dimensional printing, Solid Freeform Fabrication Symp. (1992) 244–250.
[10] S.M. Allen, E.M. Sachs, Three-dimensional printing of metal parts for tooling and other applications, Metals Mater. 6 (6) (2000) 589–594.
[11] W.H. Peter, R.R. Dehoff, P.J. Blau, Y. Yamamoto, W. Chen, A.S. Sabau, A. Klarner, Application of Wear-Resistant, Nanocomposite Coatings Produced from Iron-Based Glassy Powders, Department of Energy, Oak Ridge National Laboratory, 2013.
[12] E.E. Underwood, Quantitative Stereology, Addison-Wesley, Reading, MA, 1970.
[13] J.A. Alvarado-Contreras, E.A. Olevsky, A.L. Maximenko, R.M. German, Kinetics of shrinkage and shape evolution during liquid phase sintering of tungsten heavy alloy, J. Mater. Sci. 49 (3) (2014) 1130–1137.
[14] J.A. Alvarado-Contreras, E.A. Olevsky, R.M. German, Modeling of gravity-induced shape distortions during sintering of cylindrical specimens, Mech. Res. Commun. 50 (2013) 8–11.
[15] P. Voorhees, M. Glicksman, Ostwald ripening during liquid phase sintering—Effect of volume fraction on coarsening kinetics, Metall. Trans. A 15 (6) (1984) 1081–1088.
[16] T. Courtney, Microstructural evolution during liquid phase sintering: Part II. Microstructural coarsening, Metall. Trans. A 8 (5) (1977) 685–689.
[17] J.S.C. Jang, C.C. Koch, The Hall-Petch relationship in nanocrystalline iron produced by ball milling, Scripta Metall. Mater. 24 (8) (1990) 1599–1604.
[18] W.C. Leslie, The Physical Metallurgy of Steels, Hempishere Publishing Corporation, India, 1981.
[19] F.A. McClintock, A.S. Argon, Mechanical Behavior of Materials, Addison-Wesley, Reading, MA, 1966.